Please provide feedback

Please support the ScholarWorks@UMBC repository by emailing scholarworks-group@umbc.edu and telling us what having access to this work means to you and why it's important to you. Thank you.

CrossMark

Three Red Suns in the Sky: A Transiting, Terrestrial Planet in a Triple M-dwarf System at 6.9 pc

Jennifer G. Winters[1], Amber A. Medina[1], Jonathan M. Irwin[1], David Charbonneau[1], Nicola Astudillo-Defru[2],
Elliott P. Horch[3], Jason D. Eastman[1], Eliot Halley Vrijmoet[4], Todd J. Henry[5], Hannah Diamond-Lowe[1],
Elaine Winston[1], Thomas Barclay[6,7], Xavier Bonfils[8], George R. Ricker[9], Roland Vanderspek[9], David W. Latham[1],
Sara Seager[10,11,12], Joshua N. Winn[13], Jon M. Jenkins[14], Stéphane Udry[15], Joseph D. Twicken[14,16],
Johanna K. Teske[17,26], Peter Tenenbaum[14,16], Francesco Pepe[15], Felipe Murgas[18,19], Philip S. Muirhead[20], Jessica Mink[1],
Christophe Lovis[15], Alan M. Levine[9], Sébastien Lépine[4], Wei-Chun Jao[4], Christopher E. Henze[14], Gábor Furész[9],
Thierry Forveille[8], Pedro Figueira[21,22], Gilbert A. Esquerdo[1], Courtney D. Dressing[23], Rodrigo F. Díaz[24,25],
Xavier Delfosse[8], Christopher J. Burke[9], François Bouchy[15], Perry Berlind[1], and Jose-Manuel Almenara[8]

[1] Center for Astrophysics Harvard & Smithsonian, 60 Garden Street, Cambridge, MA 02138, USA; jennifer.winters@cfa.harvard.edu
[2] Departamento de Matemática y Física Aplicadas, Universidad Católica de la Santísima Concepción, Alonso de Rivera 2850, Concepción, Chile
[3] Department of Physics, Southern Connecticut State University, 501 Crescent Street, New Haven, CT 06515, USA
[4] Department of Physics and Astronomy, Georgia State University, Atlanta, GA 30302-4106, USA
[5] RECONS Institute, Chambersburg, PA 17201, USA
[6] NASA Goddard Space Flight Center, 8800 Greenbelt Road, Greenbelt, MD 20771, USA
[7] University of Maryland, Baltimore County, 1000 Hilltop Circle, Baltimore, MD 21250, USA
[8] Université Grenoble Alpes, CNRS, IPAG, F-38000 Grenoble, France
[9] Department of Physics and Kavli Institute for Astrophysics and Space Science, Massachusetts Institute of Technology, Cambridge, MA 02139, USA
[10] Department of Physics and Kavli Institute for Astrophysics and Space Research, Massachusetts Institute of Technology, Cambridge, MA 02139, USA
[11] Department of Earth, Atmospheric and Planetary Sciences, Massachusetts Institute of Technology, Cambridge, MA 02139, USA
[12] Department of Aeronautics and Astronautics, MIT, 77 Massachusetts Avenue, Cambridge, MA 02139, USA
[13] Department of Astrophysical Sciences, Princeton University, Princeton, NJ 08544, USA
[14] NASA Ames Research Center, Moffett Field, CA 94035, USA
[15] Observatoire de Genève, Université de Genève, 51ch. des Maillettes, 1290 Sauverny, Switzerland
[16] SETI Institute, Moffett Field, CA 94035, USA
[17] Observatories of the Carnegie Institution for Science, 813 Santa Barbara Street, Pasadena, CA 91101, USA
[18] Instituo de Astrofísica da Canarias (IAC), E-38205 La Laguna, Tenerife, Spain
[19] Departamento de Astrofísica, Universidad de La Laguna (ULL), E-38206 La Laguna, Tenerife, Spain
[20] Department of Astronomy & The Institute for Astrophysical Research, Boston University, 725 Commonwealth Avenue, Boston, MA 02215, USA
[21] European Southern Observatory, Alonso de Córdova 3107, Vitacura, Región Metropolitana, Chile
[22] Instituto de Astrofísica e Ciências do Espaço, Universidade do Porto, CAUP, Rua das Estrelas, 4150-762 Porto, Portugal
[23] Astronomy Department, University of California, Berkeley, CA 94720, USA
[24] Universidad de Buenos Aires, Facultad de Ciencias Exactas y Naturales, Buenos Aires, Argentina
[25] CONICET - Universidad de Buenos Aires, Instituto de Astronomía y Física del Espacio (IAFE), Buenos Aires, Argentina

Abstract

We present the discovery from *Transiting Exoplanet Survey Satellite* (*TESS*) data of LTT 1445Ab. At a distance of 6.9 pc, it is the second nearest transiting exoplanet system found to date, and the closest one known for which the primary is an M dwarf. The host stellar system consists of three mid-to-late M dwarfs in a hierarchical configuration, which are blended in one *TESS* pixel. We use MEarth data and results from the Science Processing Operations Center data validation report to determine that the planet transits the primary star in the system. The planet has a radius of $1.38^{+0.13}_{-0.12} R_{\oplus}$, an orbital period of $5.35882^{+0.00030}_{-0.00031}$ days, and an equilibrium temperature of 433^{+28}_{-27} K. With radial velocities from the High Accuracy Radial Velocity Planet Searcher, we place a 3σ upper mass limit of 8.4 $M_{\oplus}$ on the planet. LTT 1445Ab provides one of the best opportunities to date for the spectroscopic study of the atmosphere of a terrestrial world. We also present a detailed characterization of the host stellar system. We use high-resolution spectroscopy and imaging to rule out the presence of any other close stellar or brown dwarf companions. Nineteen years of photometric monitoring of A and BC indicate a moderate amount of variability, in agreement with that observed in the *TESS* light-curve data. We derive a preliminary astrometric orbit for the BC pair that reveals an edge-on and eccentric configuration. The presence of a transiting planet in this system hints that the entire system may be co-planar, implying that the system may have formed from the early fragmentation of an individual protostellar core.

Key words: binaries: close – planets and satellites: detection – stars: individual (LTT 1445) – stars: low-mass

1. Introduction

Until the advent of large space missions capable of spatially resolving rocky planets from their host stars, the only terrestrial exoplanets that will be spectroscopically accessible will be those that orbit nearby, mid-to-late M dwarfs (National Academies of Sciences & Medicine 2018). Transiting examples of such planets are particularly advantageous, as they allow the unambiguous determination of masses, radii, mean densities, and surface gravities, and permit their atmospheres to be

---
[26] Hubble Fellow.

probed using the technique of transmission spectroscopy. Yet even with the large apertures of upcoming facilities, such studies will be photon starved: it may be possible to search for molecular oxygen in the atmospheres of terrestrial exoplanets with the upcoming cohort of ground-based giant, segmented mirror telescopes (GSMTs), but studies indicate that even marginal detections will be feasible only for stars within 15 pc and no larger than $0.3\,R_\odot$ (Snellen et al. 2013; Rodler & López-Morales 2014; López-Morales et al. 2019). The eagerly awaited *James Webb Space Telescope* (*JWST*) may also be able to detect key molecules such as water, methane, and carbon dioxide in the atmospheres of terrestrial exoplanets, but again demands parent stars that are similarly nearby, and small (Morley et al. 2017).

Within 15 pc, there are 411 M dwarfs with masses between 0.3 and $0.1\,M_\odot$, and perhaps an additional 60 systems between $0.1\,M_\odot$ and the main-sequence cut-off (Winters et al. 2018a, 2019; Bardalez Gagliuffi et al. 2019). How many transiting terrestrial worlds might we expect within this sample of stars? Dressing & Charbonneau (2015) analyzed the data from the *Kepler* mission and found that, on average, M dwarfs host 2.5 planets smaller than $4\,R_\oplus$ with periods less than 200 days. Considering only planets with radii between 1.0 and $1.5\,R_\oplus$ and periods less than 50 days, they found a mean number of planets per M dwarf of 0.56. Importantly, these stellar primaries were typically early M dwarfs, roughly twice as massive as the mid-to-late M dwarfs required to enable the atmospheric studies described above. Although efforts are underway to use *K2* data to determine the rate of planet occurrence for the less massive M dwarfs (e.g., Dressing et al. 2019), it is currently an open question whether they host small planets with the same frequency as their more massive counterparts.

For stars less massive than $0.3\,M_\odot$ and within 15 pc, four families of transiting, terrestrial planets are known: GJ 1132bc (Berta-Thompson et al. 2015; Bonfils et al. 2018), LHS 1140bc (Dittmann et al. 2017; Ment et al. 2019), TRAPPIST-1bcdefgh (Gillon et al. 2016, 2017; Grimm et al. 2018), and LHS 3844b (Vanderspek et al. 2019). Yet the closest of these lies at 12 pc, for which the *JWST* and the GSMTs may still be at pains to access. Thus, there is great interest within the community to identify even closer examples of such systems.

The *Transiting Exoplanet Survey Satellite* (*TESS*; Ricker et al. 2015) mission is now one year into its two year prime mission to scan most of the sky in search of the transiting planets that are most amenable to follow-up study. We report here the detection with *TESS* data of the second closest known transiting exoplanet system, LTT 1445ABC (TIC 98796344, TOI 455), and the nearest one for which a terrestrial planet transits a low-mass star. The planet is 6.9 pc away, and orbits one member of a stellar triplet. Multi-star systems present numerous challenges which sometimes deter planet hunters: astrometric perturbations from stellar companions at small separations can hinder the measurement of the trigonometric parallax of the system; the presence of bound companions can result in trends in the radial velocities (RVs) of a star that can mask the signals of planets; and light contamination from close stellar companions in the photometry of a host star can result in an underestimated planet radius (Ciardi et al. 2015; Furlan & Howell 2017; Hirsch et al. 2017). Yet these complications are also opportunities to measure the stellar orbits and investigate the potential formation scenarios for the planets that are found within; indeed all of these features are present in the system

that is the subject of our study. We present here the discovery of the planet and a description of the host star system. We first provide a detailed portrait of the host star system in Section 2. We then detail the observations in Section 3. In Section 4, we present our analysis of the data. Finally, in Section 5 we discuss the implications of this planet and the opportunity it presents for characterization of its atmosphere.

2. Description of the Host Stellar System

The host system, LTT 1445ABC (Luyten 1957, 1980), is a nearby, hierarchical trio of mid-to-late M dwarfs. Rossiter (1955) is the first observer to have noted relative astrometry for LTT 1445ABC using visual micrometry. In two observations made near the beginning of 1944 (specifically, Besselian years 1943.960 and 1944.027), the primary star was measured to have a separation from the B component of $3''03$ and $3''51$. In those same observations, the BC subsystem was measured to have a separation of approximately $1''3$. Since then, the separation of the primary relative to the subsystem has increased to a maximum value of $7''706$ in 2003 (Dieterich et al. 2012), and is now apparently decreasing, with the most recent value of $7''10$ obtained in 2017, according to data available in the Washington Double Star (WDS) Catalog[27] (Mason et al. 2001). In contrast, for much of the time since 1944, the BC subsystem has been on a trajectory of decreasing separation; however, the most recent speckle observations appear to show that this trend has now reversed, and the separation is growing larger. As shown in Figure 1, the three components are visible in an archival *Hubble Space Telescope* (*HST*) NICMOS image (left panel), but the B and C components are blended in our ground-based image from MEarth-South (right panel).

As reported by Henry et al. (2018) with over 18 years of RECONS[28] astrometry data, the position of the primary star exhibits an astrometric perturbation due to the presence of the BC pair. We describe a preliminary orbit for the BC pair below in Section 2.1.

Because of the nearly equal brightnesses of the A and blended BC components of the system, there has been confusion in the literature regarding their designations. Convention dictates that the primary component is the brightest in the *V* filter and is therefore the most massive of all stars in a multiple system.[29] The confusion appears to have originated with Luyten, who may not have been aware of Rossiter's work on this system. The Luyten Two Tenths Catalogue (Luyten 1957) lists only one entry for the system, but the New Luyten Two Tenths Catalogue (Luyten 1980) lists two entries with identical coordinates and proper motions. The brighter star ($m_R = 11.1$ mag, $m_{pg} = 12.7$ mag) is noted as LP 771-95; the fainter star ($m_R = 11.8$ mag, $m_{pg} = 13.5$ mag) is noted as LP 771-96. The entry for LP 771-96 includes the note, "Comp. to 95, 121°, $4''5$," which implies that the secondary is the southeast component. The WDS entry for this result has been edited so that the position angle between the primary and secondary is 301°, presumably to bring it into agreement with results from Rossiter who had already resolved the brighter component into a stellar pair. For the remainder of this paper,

---
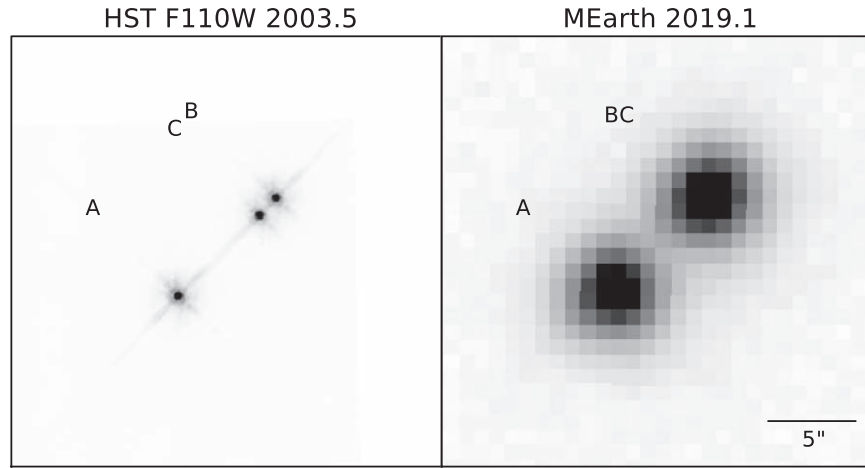
Figure 1. LTT 1445ABC. Left: *HST* NICMOS image in the F110W filter taken in 2003; Right: MEarth image taken in 2019. North is up, east is left. The BC pair are blended in the ground-based MEarth image. We note that all three components fall on one $21''$ square *TESS* pixel.

we refer to the stellar system as LTT 1445ABC, where A is the southeast component and BC is the blended northwest component.

While LTT 1445A[30] is brighter than LTT 1445BC in the *V* filter, the opposite is true in the *K* filter. Thus, if one were unaware of the binarity of the B component, mass estimates calculated using a mass–luminosity relation (MLR) will be discrepant, depending on which filter relation is used: the A component will be more massive with a *V*-band MLR calculation, while the B component will be more massive with a *K*-band MLR calculation. However, we know that LTT 1445BC[31] is a subarcsecond binary with both optical and infrared delta-magnitudes (Δmag) reported in the literature. Once the photometry of the BC components is deblended into their individual photometric magnitudes, their overluminosity in the infrared is resolved and the A component is the brightest and most massive star in the system in both the optical and infrared filters.

We calculated the *TESS* magnitudes, *T*, for all three components from $(I_{\rm KC} - K_{\rm s})$ colors[32] using relations appropriate for M dwarfs developed by G. Torres (private communication). The transformation is valid for M dwarfs with near-solar metallicity ($-1.0 \leqslant [{\rm Fe/H}] \leqslant 0.5$) and has a residual scatter of 0.013 mag. We provide the relation as

$$T = I - 1.2457 + 1.54056 * (I - K)$$
$$- 0.49790 * (I - K)^2 + 0.04539 * (I - K)^3.$$

The transformation from $(I - K)$ to T for the primary star was straightforward. For the secondary pair, we first deblended the *I*- and *K*-band magnitudes using Δmags reported in the literature: ΔI of 0.66 ± 0.07 mag by Henry et al. (2006) and ΔK of 0.52 ± 0.03 mag, which we calculated by averaging the values of ΔF207M and ΔF222M by Dieterich et al. (2012). We also deblended the *V*- and *R*-band photometry. We list the stellar system parameters in Table 1.

2.1. Orbit Calculation of LTT 1445BC

We used the high-resolution astrometry of observations appearing in the Fourth Interferometric Catalog[33] (FIC), plus the addition of previously unpublished data using the Differential Speckle Survey Instrument (DSSI) speckle camera (Horch et al. 2009) at the WIYN telescope in 2012, to compute a preliminary visual orbit for the BC subsystem. Table 2 lists the observations used in the orbit calculation, including previously published DSSI observations of this pair (Horch et al. 2015, 2017). Only data from 2003 to the present were used; data before this did not use high-resolution techniques, and therefore the astrometry would generally be of lower precision. We used the method of MacKnight & Horch (2004), which takes as input an upper limit and a lower limit for each of the seven orbital elements and first computes a grid search to find the elements within the ranges selected that minimize the squared observed-minus-predicted differences in the secondary's position. After those elements are found, a second calculation is done to refine those orbital elements using the downhill simplex algorithm. Uncertainties in orbital elements are estimated by adding Gaussian random deviations of the expected astrometric uncertainty to all of the observed position angles and separations and recomputing the orbit many times. This yields a sample distribution for each orbital element; the uncertainty is calculated to be the standard deviation of the distribution in each case.

A reanalysis of the 2014 DSSI data indicates that the quadrant of the secondary in those images is ambiguous, a situation that can arise in speckle imaging when observing fainter targets. Using the position angle values shown in the FIC results in an orbit that is highly eccentric ($e = 0.9$) and implies a mass sum for the BC subsystem of 0.63 ± 0.28 solar masses. On the other hand, if one reverses the quadrant of those observations by adding 180 degrees to the position angle, the derived parameters indicate that the pair has a somewhat eccentric, edge-on orbit with a period of roughly 36 yr. While either orbit is possible, at this point we judge the latter as more likely because the residuals to the orbit fit are significantly smaller. We list the orbital elements derived in that case in Table 3. Because the data span only 11 yr (roughly one-third of

---

[30] Other names: TIC 98796344, TOI 455, L 730-18, BD-17 588A, RST 2292A, WDS J03019-1633A, 2MASS J03015142-1635356, Gaia DR2 5153091836072107136.

[31] Other names: TIC 98796342, BD-17 588B, RST 2292BC, WDS J03019-1633B, 2MASS J03015107-1635306, Gaia DR2 5153091836072107008.

[32] Henceforth, we omit the subscripts on these filters. The central wavelengths are 8075 Å and 2.159 μm for the *I* and *K* filters, respectively.

[33] https://www.usno.navy.mil/USNO/astrometry/optical-IR-prod/wds/int4

Table 1
System Parameters for LTT 1445ABC

Parameter	A	BC	B-deblended	C-deblended	Reference
R.A. (2000.0) (hh:mm:ss)	03:01:51.39	03:01:51.04	…	…	3, 3
Decl. (2000.0) (dd:mm:ss)	−16:35:36.1	−16:35:31.1	…	…	3, 3
Proper motion mag. (mas yr^{-1})	456.5 ± 0.2	479.4 ± 0.3	…	…	2, 3
Proper motion PA (deg)	234.0 ± 0.07	234.1 ± 0.08	…	…	2,3
Parallax (mas)	145.55 ± 0.08	142.57 ± 2.03	…	…	2, 3, 3
T (mag)	8.88 ± 0.02	8.80 ± 0.02J	9.27 ± 0.07	9.92 ± 0.07	1, 1, 1, 1
V_J (mag)	11.22 ± 0.02	11.37 ± 0.03J	11.78 ± 0.09	12.64 ± 0.09	3, 3, 1, 1
R_{KC} (mag)	10.07 ± 0.02	10.13 ± 0.02J	10.57 ± 0.04	11.32 ± 0.04	3, 3, 1, 1
I_{KC} (mag)	8.66 ± 0.02	8.58 ± 0.02J	9.05 ± 0.07	9.71 ± 0.07	3, 3, 1, 1
J (mag)	7.29 ± 0.02	7.11 ± 0.02J	…	…	4, 4
H (mag)	6.77 ± 0.04	6.56 ± 0.02J	…	…	4, 4
K_S (mag)	6.50 ± 0.02	6.29 ± 0.02J	6.81 ± 0.04	7.33 ± 0.04	4, 4
Mass ($M_\odot$)	0.257 ± 0.014	…	0.215 ± 0.014	0.161 ± 0.014	1, 1, 1
Radius ($R_\odot$)	0.268 ± 0.027	…	0.236 ± 0.027	0.197 ± 0.027	1, 1, 1

Note. "J" indicates that the listed parameter is "joint" and includes both the B and C components.
References. (1) This work; (2) Gaia Collaboration et al. (2018); (3) Henry et al. (2018); (4) Skrutskie et al. (2006).

Table 2
Astrometry and Photometry for Observations Used in the Orbit Calculation for LTT 1445BC

Date	θ (°)	ρ (″)	Δm (mag)	λ (nm)	$\Delta\lambda$ (nm)	Tel. Dia. (m)	Technique	Reference
2003.4620	138.1	1.344	0.56	1797	68	2.4	*HST* NICMOS	2
2008.7675	137.7	0.7305	1.4	551	22	4.1	Speckle	6
2010.594	138.41	0.41	0.52	2150	320	3.0	AO	5
2012.0963	141.8	0.1812	2.16	692	40	3.5	Speckle	4
2012.0963	140.0	0.1777	1.80	880	50	3.5	Speckle	4
2012.7516	146.5	0.0710	1.05	692	40	3.5	Speckle	1
2012.7516	141.4	0.0694	0.87	880	50	3.5	Speckle	1
2014.7557	316.1[a]	0.2838	1.47	692	40	4.3	Speckle	3
2014.7557	316.6[a]	0.2824	1.03	880	50	4.3	Speckle	3

Note.
[a] Quadrant ambiguous; the position angle here has been changed by 180 degrees relative to the original result.
References. (1) This paper; (2) Dieterich et al. (2012); (3) Horch et al. (2015); (4) Horch et al. (2017); (5) Rodriguez et al. (2015); (6) Tokovinin et al. (2010).

Table 3
Preliminary Orbital Parameters for LTT 1445BC

| Parameter	Value
Orbital period (yr)	36.2 ± 5.3
Semimajor axis (arcseconds)	1.159 ± 0.076
Inclination (deg)	89.64 ± 0.13
Ω (deg)	137.63 ± 0.19
T_0 (Besselian year)	2019.2 ± 1.7
Eccentricity	0.50 ± 0.11
ω (deg)	209 ± 13

the orbital period shown in Table 3), this results in large uncertainties in some of the orbital elements, particularly the semimajor axis and the period. High-quality orbital elements are not likely to be obtained for another decade, when it is hoped observations will be available to clearly show the orbital progress. We show the visual orbit we have calculated in Figure 2. We show the ephemeris predictions and residuals for all observations used in the orbit calculation in Table 4.

Despite the very tentative nature of this orbit, the inclination is already very well constrained and the speckle data points have residuals that are fairly consistent with the known measurement

precision of the technique; typical measurement uncertainties would be in the range of 2–3 mas in separation, and 0°.5–1° in position angle at the telescope used, for example. Using the *Gaia* DR2 parallax reported for the primary star and the orbital results for period and semimajor axis, we derive a total mass for the BC subsystem of $0.39 \pm 0.09\,M_\odot$. The uncertainty in the mass is calculated from the independent trials of the orbit described above. Each trial gives a period and semimajor axis, and each is used, together with a randomly chosen parallax deviate from a Gaussian distribution of the same mean of the *Gaia* parallax and standard deviation of the *Gaia* parallax uncertainty. The standard deviation of these mass values is our estimate of the mass uncertainty. This result is consistent with the sum of the masses estimated from the mass–M_K relation (Benedict et al. 2016) using the deblended K-band photometry ($0.221 \pm 0.014 + 0.165 \pm 0.014\,M_\odot = 0.386 \pm 0.020\,M_\odot$). Using the total mass of the three stellar components and an average angular separation of 5″ (corresponding to 34 au), we estimate the period of the A–BC orbit to be roughly 250 yr. No further analysis of this orbit has been done.

Photometric information on the BC pair is difficult to interpret at this stage. Henry et al. (2006) noted a decrease in brightness of 0.3 magnitudes in a blended image taken in 1999. This was one of a series of observations taken as a part of the
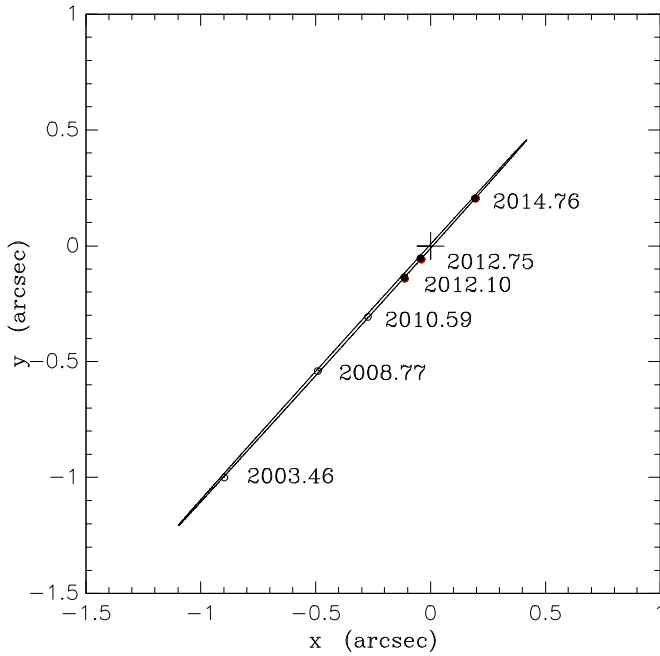
Figure 2. Preliminary astrometric orbit of LTT 1445C relative to LTT 1445B. Data points appearing in the Fourth Interferometric Catalog are shown with open circles. The three pairs of observations obtained with DSSI are shown as filled circles, with red indicating the 692 nm filter and black indicating the 880 nm filter. The cross indicates the position of LTT 1445B. North is up; east is left.

Date	θ_{eph} (deg)	ρ_{eph} ('')	$\Delta\theta$ (deg)	$\Delta\rho$ ('')
2003.4620	137.9	1.3452	0.2	−0.0012
2008.7675	138.3	0.7166	−0.6	0.0139
2010.594	138.7	0.4320	−0.3	−0.0220
2012.0963	140.1	0.1786	1.7	0.0026
2012.0963	140.1	0.1786	−0.1	−0.0009
2012.7516	144.2	0.0648	2.3	0.0062
2012.7516	144.2	0.0648	−2.8	0.0046
2014.7557	316.4	0.2821	−0.3	0.0017
2014.7557	316.4	0.2821	0.2	0.0003

RECONS parallax effort, and those authors suggested that they had viewed a potential eclipsing event. The Tokovinin et al. (2010) measure from 2008 notes the magnitude difference obtained is of reduced quality. In the recent sequence of speckle measures with the DSSI speckle instrument, including the measures presented here from 2012 October, there are three measures of the magnitude difference in both 692 nm and 880 nm filters, but they have large scatter. Computing the average and standard error from these measurements, we obtain $\Delta 692\,\mathrm{nm} = 1.56 \pm 0.32$ and $\Delta 880\,\mathrm{nm} = 1.23 \pm 0.29$. These values carry larger uncertainty than expected; more observations are warranted.

3. Observations

3.1. TESS

LTT 1445A and BC were observed by *TESS* in sector four from UT 2018 October 19 to November 15, in spacecraft orbits 15 and 16. The observations were acquired with CCD 4 on Camera 2. We included this system in our *TESS* Guest Investigator program (PI Winters; G011231) target list to gather short-cadence (two minute) data of the volume-complete sample of mid-to-late M dwarfs within 15 pc. LTT 1445A and BC were also included in the *TESS* Input Catalog (TIC) and Candidate Target List (CTL) (Stassun et al. 2018) via the Cool Dwarf Sample (Muirhead et al. 2018).

The two minute cadence data were reduced with the NASA Ames Science Processing Operations Center (SPOC) pipeline (Jenkins et al. 2015, 2016) which was repurposed from the *Kepler* reduction pipeline (Jenkins et al. 2010). A planetary candidate with radius $1.4 \pm 0.4\,R_\oplus$ was detected based on four transits to have a period of 5.4 days and a transit depth of 2498 ± 168 ppm with a signal-to-noise ratio of 15.4.

As noted in the data release notes[34] for sector 4, this was the first sector to benefit from the improved Attitude Control System algorithm, which reduced the pointing jitter of the spacecraft by an order of magnitude over the pointing errors evident in data from sectors 1–3. Two anomalies were noted in sector 4. An incorrect guide star table was initially used; when the correct guide star table was uploaded, the spacecraft pointing shifted by 4''. All cameras showed a maximum attitude residual of about 0.45 pixels that decreased to roughly 0.2 pixels once the guide star catalog was updated. In addition, communications between the spacecraft and instrument ceased for roughly 64 hr (between times 2458418.54 and 2458421.21), during which time no telemetry or data were collected.

The *TESS* light curve, shown in Figure 3, shows various types of stellar variability, such as flares and rotational modulation due to spots. We estimate a rotation period of 1.4 days from the *TESS* light curve (described in more detail in Section 4.3.1), which we suspect originates from either the B or C component, based on the activity indicator measurements for A and BC from our Tillinghast Reflector Echelle Spectrograph (TRES) spectra (described below). The duty cycle of the flares is fairly low, and those that occur are rather weak, with an increase in brightness on the order of 4% (roughly 40 mmag); however, one large flare was detected, as seen in the top panel of Figure 3, similar to the one reported by Howard et al. (2019). While we do not know from which star the flares originate, previous work indicates that rapidly rotating stars flare more frequently. Thus, we suspect that the flares, too, come from either or both of the B or C components.

3.2. Photometric Follow-up with MEarth-South

The large *TESS* pixel size of 21'' means that the two nearly equal-luminosity sources, A and the blended BC, are included in the *TESS* aperture. Therefore it was necessary to determine from which star the transit signal originated. We obtained follow-up observations with MEarth-South for this purpose. One transit ingress of LTT 1445Ab was observed using four telescopes of the MEarth-South array at Cerro Tololo Inter-American Observatory (CTIO), Chile, on UT 2019 February 16. Exposure times were 4 s, with a total of 1445 data points gathered over 3 hr at airmasses 1.2–3.0 starting immediately at twilight until the target set. Due to the combination of the short exposure time and high airmass, particularly at transit ingress

---

[34] https://archive.stsci.edu/missions/tess/doc/tess_drn/tess_sector_04_drn05_v04.pdf
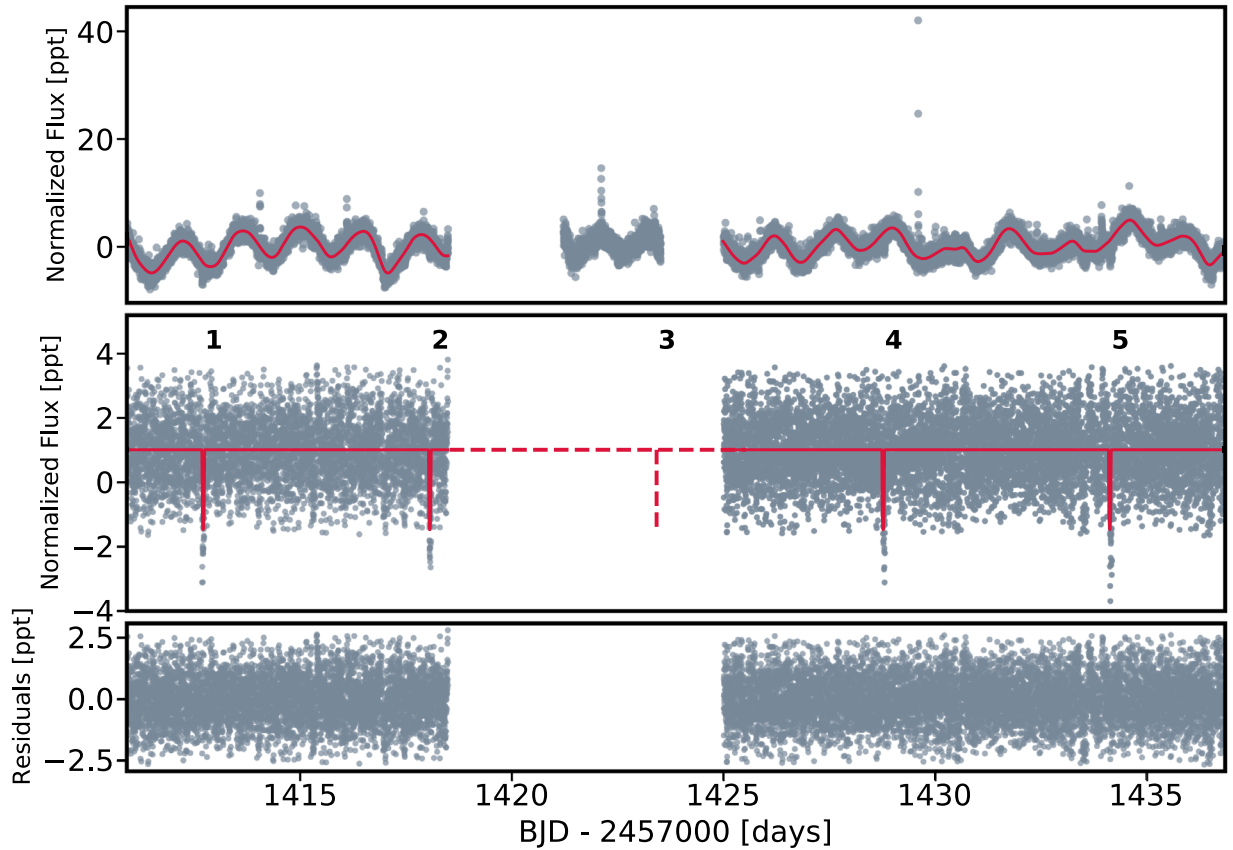
Figure 3. *TESS* Pre-Search Data Conditioning Simple Aperture Photometry light curve. The top panel shows evidence of flares and rotational modulation due to stellar spots, likely on either the B or C component. The solid (crimson) line indicates the fit to the modulation. The middle panel shows the residual data after the removal with Gaussian Processes (GPs) of the stellar variability; the planetary transit model is overplotted (solid crimson line) and the number for each transit is indicated. The dotted line indicates the third transit, which was not included in our fit. The bottom panel illustrates the light curve with planetary transit and stellar variability removed. The description of the flare rejection and GP fitting are given in Section 4.3.1.

and thereafter, these data show very high levels of noise due to atmospheric scintillation. Two of the telescopes used in this observation had shutters stuck in the open position, and as a result the images were smeared during readout, but this does not appear to affect the resulting differential photometry.

The FWHM of the stellar images ranged from approximately 2.0–3.5 pixels, with a plate scale of 0.84 arcsec pixel^{-1}. These observations resolve A from BC, but the wings of the point-spread functions are still mildly overlapping and require specialized reduction procedures. In order to mitigate the influence of aperture positioning errors, the global astrometric solutions for the images were used for aperture placement (e.g., as described by Irwin et al. 2007), rather than individually determining the location of each star from the individual images. Undersized extraction apertures with radii of 4.2 pixels were used for the A and BC components, where the aperture size was chosen to prevent overlap of the apertures. Due to the lack of useful comparison stars elsewhere on the images, BC was used as the comparison source to derive differential photometry of A. The resulting light curve is shown in Figure 4. It is compatible with the transits detected by *TESS*, although with low signal-to-noise, and suggests the transits originate from A. While we acknowledge that this detection is marginal, we provide further confirmation that the planet orbits the primary component in the system in Section 4.

3.3. Reconnaissance Data

We used high-resolution data we had previously acquired as part of our ongoing, nearby M-dwarf binary surveys (Winters et al. 2019) to confirm that the host star has no additional stellar or brown dwarf companions at separations less than 50 au. We also investigated its rotational broadening and measured the equivalent width of Hα. In addition, we used roughly two decades of RECONS data from the CTIO/SMARTS 0.9 m telescope to explore the system's long-term variability.

3.3.1. High-resolution Speckle Imaging: DSSI

As part of our all-sky speckle survey of 1000 nearby M dwarfs for stellar companions (Winters, in prep), we observed LTT 1445A on UT 2016 January 18 using DSSI on the Gemini-North 8.1 m telescope. One thousand 40 ms exposures were taken in two filters (centered at 692 and 880 nm) simultaneously. This group of frames was followed by a similar set of exposures for a bright, unresolved calibration star at close proximity on the sky to the science star. The data reduction and analysis were conducted as described by Horch et al. (2017).

We show the contrast curves for the 692 nm (left panel) and 880 nm (right panel) filters in Figure 5. As illustrated in the left panel, no companions to LTT 1445A were detected with Δ692 nm less than 5.06 mag at separations 0.″2–1.″2 (corresponding to projected linear separations of 1.4–8.2 au) from LTT 1445A.
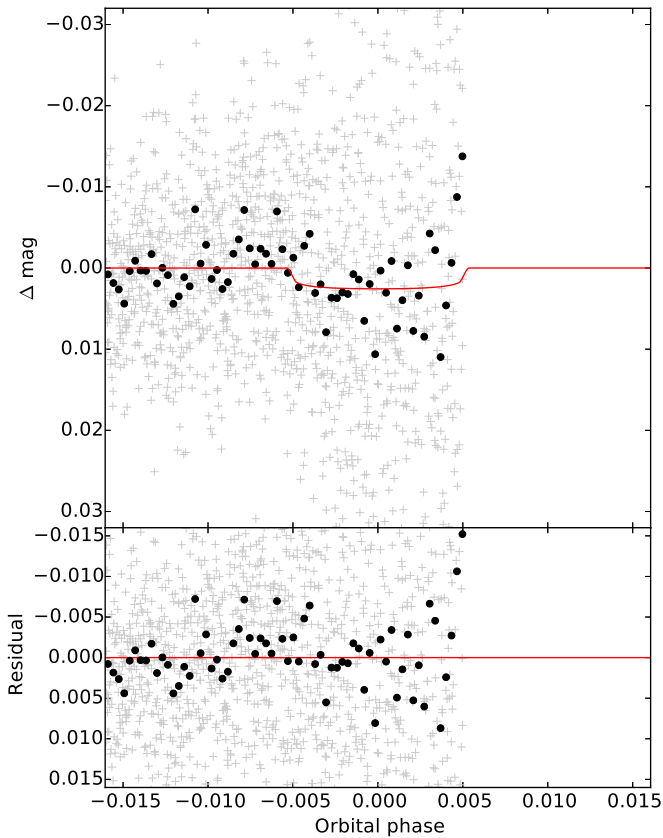
Figure 4. Partial transit event of LTT 1445Ab (top panel) observed by MEarth-South, suggesting that the transit comes from LTT 1445A. The data have been phase-folded using the final transit parameters given in Table 8. The individual data points are indicated in gray; black points indicate the data binned by 2.5 min; the red line illustrates the fit to the transit event, computed by taking the mean of the Markov chain Monte Carlo posterior parameters from Table 8. Error bars on the individual data points have been omitted for clarity, but are large due to the high airmass of the observation. Residuals to the fit are shown in the bottom panel.

Additionally, no companions were detected with $\Delta 880$ nm less than 7 mag at separations larger than $0\overset{''}{.}6$ (roughly 4.1 au). An L2 V spectral type, which we consider to be the "end of stars" (Dieterich et al. 2014), has M_I of roughly 16.0 mag. The M_I for LTT 1445A is 9.48 mag, placing constraints to M_I of 16.48 mag on the presence of a companion at separations greater than $0\overset{''}{.}6$, beyond the end of the M-dwarf sequence and into the brown dwarf regime. This is in agreement with results by Dieterich et al. (2012) who observed the system with *HST* (NICMOS) and did not detect a stellar or brown dwarf companion to the primary star.

3.3.2. High-resolution Spectroscopy: TRES

As part of our all-sky spectroscopic survey of mid-to-late M dwarfs within 15 pc, we acquired multiple high-resolution spectra of both the A and BC components with the TRES on the FLWO 1.5 m Reflector. The TRES is a high-throughput, cross-dispersed, fiber-fed echelle spectrograph with a resolving power of roughly $R = 44,000$ when using the medium fiber ($2\overset{''}{.}3$ diameter) and a passband of 310–910 nm. The observations span UT 2017 February 3 to 2018 January 24, with four spectra of the primary and three of the BC pair acquired. We integrated for 120–600 and 120–180 s and achieved signal-to-noise ratios of 16–25 and 16–21 for A and BC, respectively, at

715 nm. We used the methods described in Winters et al. (2018b) for our analysis.

The equivalent width of the Hα line and the magnitude of the rotational broadening allows differentiation between the two resolved stellar components. The primary star exhibits Hα in absorption (we measure equivalent widths of 0.14 ± 0.01 Å, 0.23 ± 0.02 Å, 0.19 ± 0.01 Å, and 0.25 ± 0.01 Å), while the BC pair shows Hα in emission (we measure equivalent widths of -1.16 ± 0.03 Å, -1.42 ± 0.03 Å, and -1.52 ± 0.03 Å). We see negligible rotational broadening ($v\sin i$) for the primary star, which allows us to place an upper limit of 3.4 km s^{-1} (half the spectral resolution of TRES) on the rotational broadening of A; we measure a $v\sin i$ of 4.4 ± 3.4 km s^{-1} for the blended secondary–tertiary pair. While we cannot rule out that the photometric modulation seen in the *TESS* light-curve data comes from A, it is more likely to come from BC because we detect both Hα in emission and rotational broadening in the spectra of those blended components. We use the relation $P_{rot} * v \sin i = 2\pi R \sin i$, the 1.4 day rotation period, and the estimated radii for each component from Table 1, to estimate rotational broadening of 9.7, 8.7, and 7.2 km s^{-1} for the primary, secondary, and tertiary components, respectively, assuming each star is viewed edge-on.

We did not detect a second pair of lines in the spectra of the primary component that would indicate the presence of an additional stellar companion to A. Using the parameters from the preliminary astrometric orbit in Table 3, we calculate an expected RV semi-amplitude of B due to C of 3.3 km s^{-1}.

3.3.3. CTIO/SMARTS 0.9 m

RECONS has been astrometrically and photometrically monitoring this system for over 19 years at the CTIO/SMARTS 0.9 m telescope. In fact, the first trigonometric parallaxes for A and BC were reported in Henry et al. (2006). These data in the *V* filter permit the investigation of the long-term variability of the system. Following the methods described in Hosey et al. (2015), we note that, over the 19 years of monitoring, the A component varies by 13.4 mmag while the BC pair vary by 13.0 mmag. While we do not consider either of these results indicative of a clearly variable source, for which we require an overall variability of 20 mmag, the levels for both are roughly twice that of the least variable M dwarfs at 7 mmag. We conclude that there are spots present on both A and the BC pair, but they do not change in coverage by an amount that alters the emergent flux in *V* by more than 2%. These results are in agreement with the moderate, short-term variability we detect in the *TESS* light-curve data.

3.4. High Accuracy Radial Velocity Planet Searcher

To constrain the mass of the transiting object, we acquired five new spectra of the primary star with the High Accuracy Radial Velocity Planet Searcher (HARPS) spectrograph (Mayor et al. 2003) on the La Silla 3.6 m telescope before the target was no longer observable. This totalled 14 spectra when combined with the nine existing spectra in the ESO HARPS archive. HARPS is a fiber-fed echelle spectrograph with resolving power $R = 115,000$ and a wavelength range of 378–691 nm. Spectra of LTT 1445A were integrated over 900 s, except for the first two spectra acquired on 2003 December 15 and 2004 November 29, where the exposure times were 572 s and 772 s, respectively. The signal-to-noise ratio ranges between 37.8 and 72.5 at
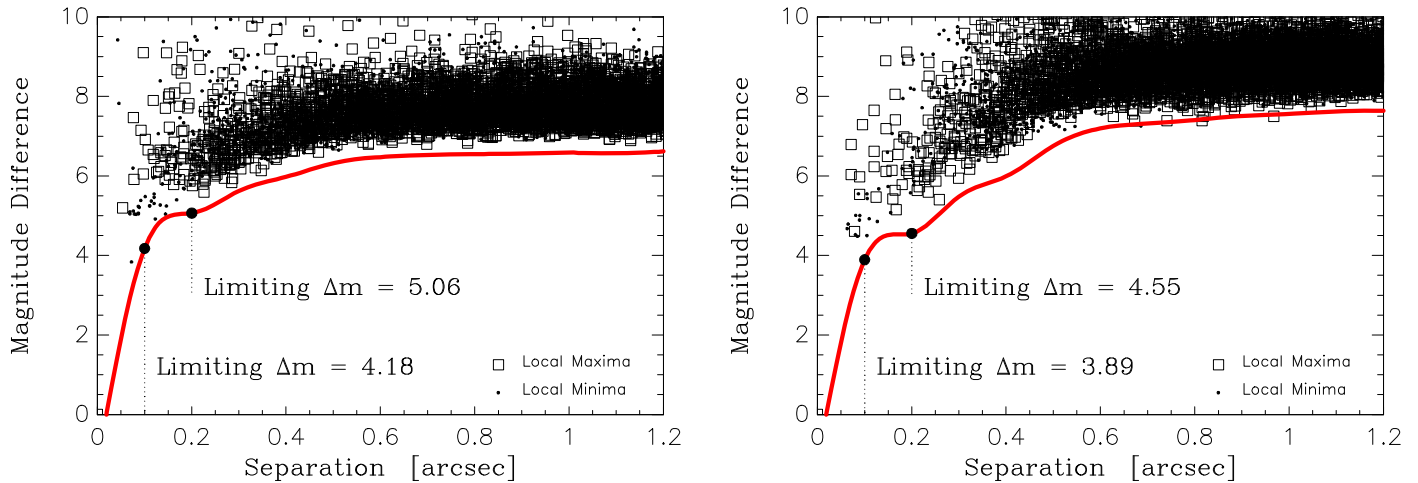
Figure 5. Contrast curves of LTT 1445A from DSSI on the Gemini-North 8.1 m in the 692 nm (left panel) and 880 nm (right panel) filters. Open squares represent the positions of local maxima in the reconstructed image and points represent local minima (where the absolute value of the minimum is used). The red line represents the 5σ line as a function of separation. The lack of points below the red line illustrates that the primary component of LTT 1445 has no companions with Δmag less than 4.55 mag at separations $0\rlap{.}''2$–$1\rlap{.}''2$ (corresponding to projected linear separations of 1.4–8.2 au) from LTT 1445A.

650 nm, with an average of 55. For these spectra, this translates into RV uncertainties (computed following Bouchy et al. 2001 and the procedure described below) ranging between 0.9 and 1.7 m s^{-1}, with an average uncertainty of 1.2 m s^{-1}.

RVs were derived by a χ^2-minimization, or so-called template matching. We briefly summarize here the implementation of the process, which is described in more detail in Astudillo-Defru et al. (2015). We first used the RVs from the HARPS pipeline (Lovis & Pepe 2007), in combination with the barycentric corrections, to shift all spectra of LTT 1445A to the solar system barycentric reference frame. We constructed an initial stellar template by computing the median of the shifted and stacked spectra. A telluric template was constructed by Doppler-shifting the observed spectra of LTT 1445A to the laboratory rest frame, which aligns the telluric absorption features, and computing the median. An improved stellar template was then constructed with the known telluric lines removed; that is, the template is a true spectrum of the star itself with improved signal-to-noise ratio. Due to the low number of spectra and to prevent auto-correlation between the stellar template and the spectrum being analyzed, contrary to Astudillo-Defru et al. (2015), we computed the stellar template for each epoch but discarded the spectrum under analysis. New RVs were then derived by minimizing the χ^2 of the residuals between the observed spectra and the stellar template. We list the RVs in Table 5.

The RVs of A exhibit a long-term drift due to the presence of the BC stellar pair, as shown in the bottom panel of Figure 7. This is in agreement with the astrometric perturbation of A due to BC mentioned above in Section 2. These precise radial-velocity data also allow us to rule out the presence of any other nearby stellar or brown dwarf object orbiting the primary star. We note that observations will continue when the system is again observable to provide a robust mass for the planet.

4. Analysis

4.1. Additional Confirmation of LTT 1445A as the Host Star

We explored a number of other methods to determine from which star the transit originates.

Table 5
HARPS Radial Velocities for LTT 1445A

BJD[a] (days)	$v_{\rm rad}$[b] (km s^{-1})	σ (km s^{-1})
2452988.689447	−5.38629	0.00174
2453338.681357	−5.39562	0.00116
2454078.640473	−5.40353	0.00105
2454080.657212	−5.40513	0.00108
2454292.913009	−5.41529	0.00091
2454316.868711	−5.41280	0.00112
2455042.915163	−5.42530	0.00088
2455997.500569	−5.43569	0.00137
2456237.681670	−5.43910	0.00130
2458546.500296	−5.45774	0.00131
2458547.501338	−5.46353	0.00116
2458548.500633	−5.46085	0.00136
2458555.506869	−5.45518	0.00129
2458556.505906	−5.45354	0.00116

Notes.
[a] Barycentric Julian date of mid-exposure, in the TDB time-system.
[b] Barycentric radial velocity.

Because our system has high proper motion, we were able to investigate whether the host star had moved on top of a background star which could be the source of the transit signal. We compared the position of the primary star in digitally scanned SuperCOSMOS (Hambly et al. 2001) archival POSS-1 images (taken 1953.93) with the star's position at the time of the *TESS* observations (we chose November 1—2018.83—the effective mid-point of sector 4). The system had moved $29\rlap{.}''6$ since the POSS-1 image was taken. No background star was seen at the current position of LTT 1445A in the POSS-1 image, which has a magnitude limit of roughly 19.5 mag at 620–670 nm.

The data validation (DV) report from the SPOC pipeline provides a number of tests to aid in analyzing planet candidates. Two of the tests in the DV report use a difference image to analyze the centroid shift that occurs during the transit event to determine from which star the transit signal originates.

The difference image provides the flux value for each pixel by taking the difference between the mean out-of-transit flux value and the mean in-transit value. Therefore, the star that is the planet host will have residual flux in the difference image. A centroid is then determined for the difference image. One analysis compares the difference image centroid to the expected position based on the TIC coordinates, while a second analysis compares the centroid of the difference image to the out-of-transit centroid. For LTT 1445ABC, the difference image centroid corresponds to LTT 1445A in both instances; however, the magnitudes of the two centroid shifts in the DV report disagree by more than a factor of three (an offset of $2\rlap{.}{''}969 \pm 0\rlap{.}{''}440$ for the TIC coordinate centroid, compared to an offset of $10\rlap{.}{''}130 \pm 0\rlap{.}{''}414$ for the out-of-transit centroid), so we investigated further. In contrast to the way this same analysis was conducted for *Kepler* objects of interest, the TIC coordinates are corrected for proper motion. Therefore, in crowded fields, the *TESS* centroid offset measurements with respect to the TIC coordinates are generally more reliable than the out-of-transit centroid. But, as noted by Twicken et al. (2010, 2018) and Stumpe et al. (2014), the out-of-transit centroid is subject to crowding and can lock on to a star that is not the target. That is, in fact, the case for LTT 1445ABC: the out-of-transit centroid position corresponds to that of the BC pair instead of the A component, resulting in an overestimated centroid offset in the DV report. Adjusting the $10\rlap{.}{''}130$ out-of-transit centroid offset by $7\rlap{.}{''}10$, the most recently measured separation of A and BC, gives an offset of $3\rlap{.}{''}03$, in agreement with the $2\rlap{.}{''}969$ offset from the TIC coordinate centroid.

In addition to the centroid shift tests, the candidate transit signature passes all the other diagnostic tests intended to flag false positives. These tests include the odd/even transit depth test, the weak secondary test, the ghost diagnostic test (which often flags background eclipsing binaries or scattered light features), and the statistical bootstrap test (false alarm probability $<3 \times 10^{-16}$).

The field is sparse. The *TESS* Exoplanet Follow-Up Observing Program entry for this system reports 10 contaminating sources, but only three additional sources are listed in the DV report and are shown to lie within the target mask. One is the nearby, physically bound pair we have discussed above (LTT 1445BC, TIC 98796342). The other two sources are faint, with reported T magnitudes of 15.032 and 15.991 at angular separations of $104\rlap{.}{''}51$ and $120\rlap{.}{''}16$ for TIC IDs 98796341 and 98796339, respectively. Our MEarth observations produced light curves for these two stars which confirm that they are not the source of the transit.

Based on the above analyses, and in combination with our marginal ground-based MEarth detection, we are confident that the planet candidate is transiting the primary star in the system.

4.2. Host Star Parameters

We use the methods appropriate for M dwarfs previously used by our group (Berta-Thompson et al. 2015; Dittmann et al. 2017; Ment et al. 2019) to determine the stellar parameters of the planet candidate host, which we then used as priors for the light-curve modeling described below. We estimate the mass of the host star using the MLR in the K band by Benedict et al. (2016) to be $0.258 \pm 0.014\,M_\odot$. The relation in M_K has been found to be less sensitive to metallicity than the M_V-band relation (Henry & McCarthy 1993; Delfosse et al. 2000; Benedict et al. 2016). For comparison, the estimated mass from the M_V-band relation

is $0.251 \pm 0.023\,M_\odot$. We then use single-star mass–radius relations (Boyajian et al. 2012) to find a stellar radius of $0.268 \pm 0.027\,R_\odot$. We calculate the bolometric correction in K using the prescription in Mann et al. (2015, erratum) to be 2.70 ± 0.04 mag, resulting in a bolometric luminosity for LTT 1445A of $0.0079 \pm 0.0003\,L_\odot$. We calculate the correction in V from Pecaut & Mamajek (2013) to be -2.06 ± 0.04 mag[35], resulting in a bolometric luminosity of $0.0082 \pm 0.0004\,L_\odot$. We adopt the mean of the two bolometric luminosities. From the Stefan–Boltzmann law, we find an effective temperature $T_{\rm eff}$ of 3337 ± 150 K. As a comparison, we also use the relations in Mann et al. (2015) to determine an effective temperature of 3332 ± 77 K for LTT 1445A, in agreement with the $T_{\rm eff}$ derived from the Stefan–Boltzmann law. We adopt the [Fe/H] of -0.34 ± 0.08 from Neves et al. (2014), which is measured from HARPS data.

4.3. Light-curve Modeling

Because of the complex nature of the light curve, we used a combination of EXOPLANET (Foreman-Mackey et al. 2017) and EXOFASTV2 (Eastman 2017) for our light-curve modeling. The purpose of using EXOPLANET was to fit and remove the photometric modulation in the *TESS* light curve using Gaussian Processes (GPs) while preserving the planetary transit signal. We then used EXOFASTV2, which does not currently have GP capability, to simultaneously fit the de-trended transit data from EXOPLANET and the HARPS RV data. EXOPLANET also has the capability to fit RV data, but we did not get convergence when including the HARPS data in the model. We elected not to include the third transit in our analysis because the light-curve baseline showed a strong slope at egress; we note that this transit was also omitted from the results in the SPOC DV report.

If there are other objects in the *TESS* aperture with TIC identifiers, the SPOC pipeline calculates a dilution (i.e., contamination) factor and performs a correction to the final light curve, as noted in the *Kepler* manual (Thompson et al. 2016). The correction for this system, contained in the keyword "CROWDSAP" in the light-curve file, is 0.485. However, the *TESS* magnitudes of 8.88 and 8.80 that we calculate for each component are slightly different from the magnitudes in the TIC and CTL (for TIC 98796344(A), $T = 8.64$ mag; for TIC 98796342(BC), $T = 8.55$ mag) because of our M-dwarf-specific relation; thus, our calculated dilution factor will be slightly different as well. From our *TESS* magnitudes, we calculated the flux for each component, from which we determined the dilution ($f_A/(f_A + f_B + f_C)$) to be 0.480 ± 0.013.

4.3.1. Exoplanet

For the first part of the light-curve analysis, we used the python package EXOPLANET (Foreman-Mackey et al. 2019). EXOPLANET employs probabilistic methods to model exoplanet transit and RV data sets. It has the additional capability to incorporate GP with CELERITE (Foreman-Mackey et al. 2017) and limb-darkened light curves with STARRY (Luger et al. 2018). We used the SPOC-generated Pre-Search Data Conditioning Simple Aperture Photometry (PDCSAP) light curve (Smith et al. 2012; Stumpe et al. 2014), corrected with our calculated dilution factor. Before fitting, we removed positive outliers (flares) deviating by more than 3.0σ above the median

---

[35] We assume the uncertainty on the bolometric correction in V is that of the $(V - K)$ color.

Table 6
EXOPLANET Planetary Orbit Parameters

Parameter	Prior[a,b]	Value	Bound
R_* ($R_\odot$)	Gaussian	$\mu = 0.268$	$\sigma = 0.013$
M_* ($M_\odot$)	Gaussian	$\mu = 0.258$	$\sigma = 0.014$
F_{*_μ} (ppt)	Gaussian	$\mu = 0.0$	$\sigma = 10.0$
u_1	Flat	0.0	(0.0–1.0)
u_2	Flat	0.0	(0.0–1.0)
T_0 (days)	Gaussian	$\mu = -0.448$	$\sigma = 0.5$
$\log P$ (days)	Gaussian	$\mu = \log 5.358$	$\sigma = 0.5$
b	Uniform	0.5	(0.0–1.0)
e	Beta	$\alpha = 0.876$, $\beta = 3.03$	(0.0–1.0)
ω	Uniform	0.0	$(-\pi - +\pi)$
$\log R_p$	Gaussian	$\mu = 0.5(\log \delta + \log R_*)$	$\sigma = 1.0$

Notes.
[a] Where μ and σ parameterize the Gaussian distribution.
[b] Where α, and β parameterize the Beta distribution.

absolute deviation of the PDCSAP light curve. To model the planetary transit, we used a limb-darkened transit model and a Keplerian orbit. The stellar variability, as well as any other possible systematics, are modeled with a GP.

We parameterized the model by the radius of the star in solar units R_*, mass of the star in solar units M_*, time of transit T_0 in days, orbital period P in days, transit impact parameter b, eccentricity e, and argument of periastron ω. This is used as the input for the light-curve modeler, STARRY, which computes a limb-darkened light curve, with parameters for quadratic limb-darkening coefficients u_1 and u_2. In addition to the limb-darkening coefficients, we parameterized the STARRY light curve by the model mentioned above, the radius of the planet R_p, the times for which the light curve is to be evaluated, the exposure time of each observation, which in our case is 120 s, and the mean of the stellar flux, F_{*_μ} in parts per thousand (ppt). We performed a box-least-squares periodogram analysis on the PDCSAP light curve in order to estimate P, T_0, and the transit depth δ. These estimates were used to inform the priors for P and T_0. We used the transit depth as a constraint on the Gaussian prior placed on the radius of the planet. The priors are summarized in Table 6.

The GP kernel is the sum of two simple harmonic oscillators:

$$\text{SHO}_1(\omega_{\text{GP}}) = \sqrt{\frac{2}{\pi}} \frac{S_1 \, \omega_1^4}{(\omega_{\text{GP}}^2 - \omega_1^2)^2 + \omega_1^2 \, \omega_{\text{GP}}^2/Q_1^2} \quad (1)$$

and

$$\text{SHO}_2(\omega_{\text{GP}}) = \sqrt{\frac{2}{\pi}} \frac{S_2 \, \omega_2^4}{(\omega_{\text{GP}}^2 - \omega_2^2)^2 + \omega_2^2 \, \omega_{\text{GP}}^2/Q_2^2} \quad (2)$$

where

$$Q_1 = 0.5 + \tau_3 + \tau_4, \quad (3)$$

$$\omega_1 = \frac{4\pi Q_1}{\tau_2 \sqrt{4Q_1^2 - 1}}, \quad (4)$$

$$S_1 = \frac{\tau_1}{\omega_1 Q_1}, \quad (5)$$

$$Q_2 = 0.5 + \tau_3, \quad (6)$$

Table 7
Gaussian Process Hyper-parameters

Hyper-parameters	Prior	Value	Bound
$\log \tau_1$ (ppt)	Gaussian	$\mu = \log \text{var(Flux)}$	$\sigma = 5.0$
$\log \tau_2$ (days)	Gaussian	$\mu = \log(1.4)$	$\sigma = 1.0$
$\log \tau_3$	Gaussian	$\mu = \log(-5.0)$	$\sigma = 1.0$
$\log \tau_4$	Gaussian	$\mu = \log(-5.0)$	$\sigma = 2.0$
τ_5	Uniform	0.0	(0.0–1.0)
$\log \tau_6$ (ppt)	Gaussian	$\mu = \log \text{var(Flux)}$	$\sigma = 10.0$

$$\omega_2 = \frac{8\pi Q_2}{\tau_2 \sqrt{4Q_2^2 - 1}}, \quad (7)$$

$$S_2 = \frac{\tau_5 \, \tau_1}{\omega_2 Q_2}. \quad (8)$$

This is an appropriate kernel for data that are quasi-periodic in nature, such as the observed rotational modulation in the light curve of LTT 1445ABC. The hyper-parameters for this GP are the amplitude of variability τ_1, the primary period of the variability τ_2, the quality factor τ_3, the difference between the quality factors of the first and second modes of the two oscillators τ_4, the fractional amplitude of the secondary mode to the primary mode τ_5, and a jitter term added to account for excess white noise τ_6. We placed a uniform prior on τ_5 and Gaussian priors on τ_1, τ_2, τ_3, τ_4, and τ_6. The mean (μ) and standard deviation (σ) value we set for the Gaussian prior on τ_1, τ_2, τ_3, τ_4, and τ_6 are shown in Table 7. For the Gaussian prior on τ_2, the primary period of variability, we estimated the mean, equal to 1.4 days, using a Lomb–Scargle periodogram of the light curve with the transits masked out.

We implemented the GP-transit model using PYMC3 (Salvatier et al. 2016). Before sampling the model, we compute an initial guess of the parameters using a built-in optimizer from EXOPLANET. The optimization finds the maximum a posteriori solution, which is used as starting values for the sampler. After an initial burn-in of 14,000 steps, 12,000 steps are drawn from the posterior. PYMC3 provides useful convergence diagnostics such as the Gelman–Rubin statistic and the number of effective samples. For each parameter in our joint GP–transit model, the Gelman–Rubin statistic was within 0.001 of 1.000 and the number of effective samples was above 4000. We show the results of our fit in Figure 3.

4.3.2. EXOFASTv2

We used the output light curve data from EXOPLANET with the stellar variability removed as input for the software package EXOFASTV2 (Eastman et al. 2013; Eastman 2017). EXOFASTV2 is a suite of IDL routines that simultaneously fits exoplanetary transit and RV data using a differential Markov chain Monte Carlo code.

Because we derived the stellar parameters as described in Section 4.2, we did not include a spectral energy distribution in the fit, and we disabled the default Modules for Experiments in Stellar Astrophysics (MESA) Isochrones and Stellar Tracks (MIST) stellar evolutionary models that use isochrones to constrain the stellar parameters. We placed Gaussian priors on the mass, radius, effective temperature, and metallicity that were equal to the uncertainties noted in Section 4.2. The quadratic limb-darkening coefficients were constrained by the TESS data and penalized for straying from the values predicted

by the Claret (2017) limb-darkening tables at a given log$g$, $T_{\rm eff}$, and [Fe/H], as is standard within EXOFASTV2. While the atmospheric models used to derive the limb-darkening tables are questionable for low-mass stars such as LTT 1445A, the impact is likely to be negligible due to the low precision of the *TESS* light curve.

As noted in Section 3.4, the 15 years of HARPS RVs exhibit a drift due to the presence of the stellar BC pair, so we included terms for the slope and quadratic curve of the RVs. Additionally, we modified the default that searches in logarithmic RV semi-amplitude space to a linear option because of the few RV measurements available. We allowed eccentricity to be a free parameter, but excluded values where eccentricity was greater than $1 - 3R_*/a$. Tides would theoretically be expected to exclude such high eccentricities because the tidal circularization timescale is very short (Adams & Laughlin 2006). In addition, the excluded eccentricities are at negative RV semi-amplitudes, which omits non-physical masses for the planet. In order to allow for the propagation of the uncertainty in the dilution which was corrected in the EXOPLANET fit, we included a prior on the correction to the dilution that was a Gaussian centered on zero with $\sigma = 0.013$. We required the number of independent draws to be greater than 1000 and and determined that, with a Gelman–Rubin statistic of 1.0107 in the worst case, the chains were well-mixed.

We find a period of $5.35882^{+0.00030}_{-0.00031}$ days, radius of $1.38^{+0.13}_{-0.12}$ $R_\oplus$, mass of $2.2^{+1.7}_{-2.1}$ $M_\oplus$, and equilibrium temperature of 433^{+28}_{-27} K for LTT 1445Ab. The equilibrium temperature assumes an albedo of zero with perfect redistribution. We show the individual transits, along with the phase-folded transit in Figure 6. In Figure 7, we show the best-fit model to the RV data, which we acknowledge is marginal. The uncertainties illustrated are the RV uncertainties from Table 5 added in quadrature with the fitted RV jitter. The uncertainty on the planet's mass is largely due to the sparse RV coverage, so we place a 3σ upper limit on the RV semi-amplitude K, planet mass, and planet density. The 3σ upper limit is where 99.73% of all links of all chains, after discarding the burn-in, are smaller than the quoted value. Listed in Table 8 are the 68% confidence values from the EXOFASTV2 fit. In addition we list the 3σ upper limits for K and its derived parameters.

To confirm that the two light-curve fitting packages produce the same result, we also ran EXOFASTV2 on the GP-corrected transit data without including the RV data. The transit-only results from EXOFASTV2 and EXOPLANET were consistent with each other, within the errors. We also compared results from a fit to the detrended, whitened (i.e., the DV time series) *TESS* light curve to our EXOPLANET + EXOFASTV2 fit results and found good agreement.

5. Discussion

To summarize, we have presented the discovery of LTT 1445Ab, which resides in a host system composed of three mid-to-late M dwarfs at 6.9 pc. The planet has a radius $1.38^{+0.13}_{-0.12}$ $R_\oplus$, an orbital period of $5.35882^{+0.00030}_{-0.00031}$ days, and an equilibrium temperature of 433^{+28}_{-27} K; we place a 3σ upper mass limit of 8.4 $M_\oplus$ on the planet. We have also presented a detailed view of the host system, which includes a preliminary orbit for the bound BC stellar pair that shows it to be in an eccentric and edge-on configuration.
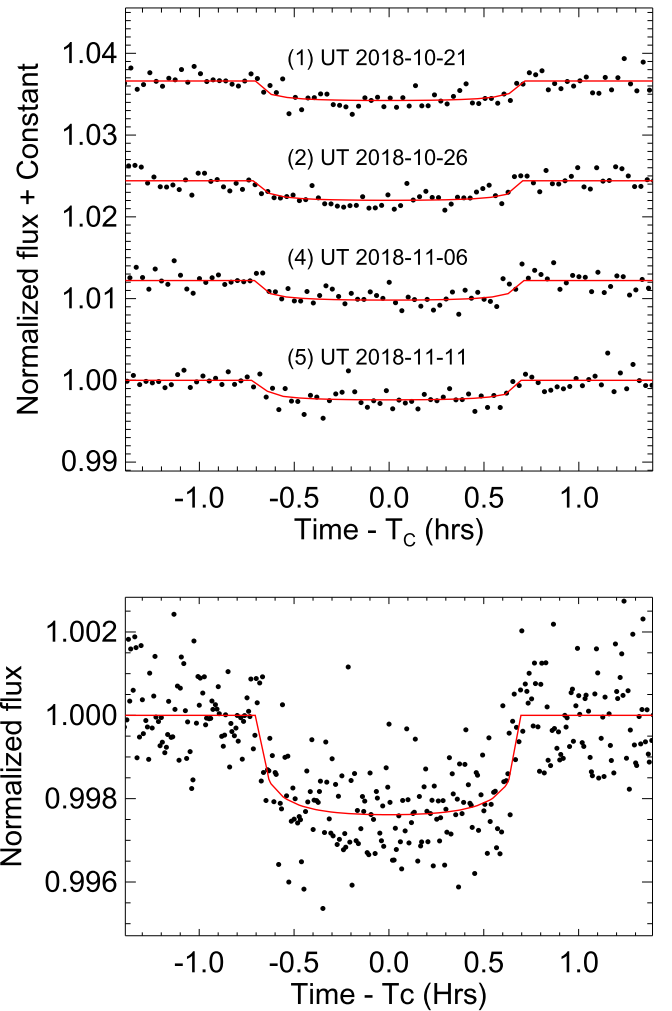
Figure 6. Transits of LTT 1445Ab from *TESS* data, fit simultaneously with the RV data using EXOFASTV2. The individual transits are shown in the top panel, where the numbers in parentheses correspond to the transit numbers in Figure 3; the phase-folded transit is shown in the bottom panel.

The planet is an S-type (satellite) planet, meaning that it orbits one component of a stellar multiple system (Dvorak 1982). Most of the literature on planets in multiple star systems considers planets in binary systems with solar-type primary stars (Eggenberger 2010; Wang et al. 2014a, 2014b; Winn & Fabrycky 2015; Kraus et al. 2016; Matson et al. 2018). Partly this is because attention has only recently shifted to M dwarfs as planet hosts. Because stellar multiplicity is known to be a decreasing function of primary mass (Duchêne & Kraus 2013), M dwarfs have a smaller stellar multiplicity rate than more massive stars: Winters et al. (2019) estimate it to be $26.8 \pm 1.4\%$, in agreement with recent results of $26 \pm 3\%$ and $28.6^{+2.7}_{-3.1}\%$ from Duchêne & Kraus (2013) and Ward-Duong et al. (2015), respectively. As a result, there are fewer systems to discuss, even if every M-dwarf system has a planet. Theoretical work has shown that planets in binary systems are in stable configurations if their separations from their host stars are less than one third of the distance to a gravitationally bound companion (Holman & Wiegert 1999). The 0.038 au separation of LTT 1445Ab is significantly less than one third of the 21 au separation between A and BC (the smallest separation measured between A and B by Rossiter in 1943). Therefore,
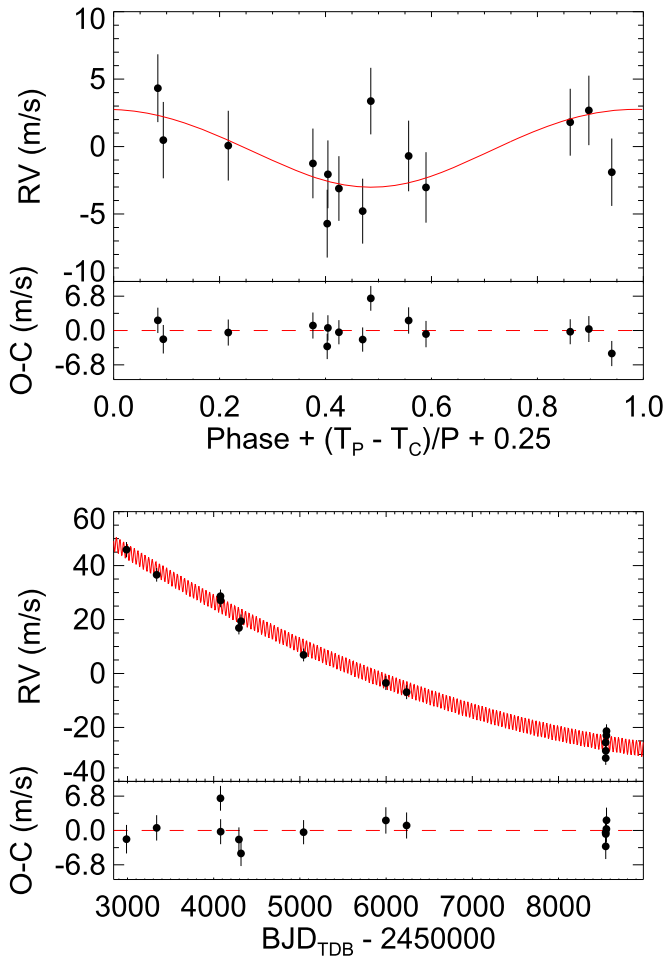
Figure 7. Preliminary spectroscopic orbit of LTT 1445Ab from HARPS data, fit simultaneously with the *TESS* transit data using EXOFASTV2. The orbit and its residuals are shown in the top panel, while the velocity drift of the primary star due to the stellar BC components is evident in the bottom panel, along with the residuals.

the planet is likely in a dynamically stable orbit, even given the presence of two other stars in the system.

M dwarfs are thought to be more likely than more massive stars to host multiple planets in compact orbits of less than roughly 10 days (Muirhead et al. 2015; Ballard 2019, respectively, for early and mid-to-late M dwarfs). LTT 1445A may very well host multiple planets but, with only one sector of data from *TESS*, we have not yet seen indications of other planets in the system.

The alignment of the three stellar components and the edge-on orbit of the BC pair and planet are suggestive of the co-planarity of the system. Including LTT 1445ABC, there are six "pure" M-dwarf triples known within 10 pc.[36] Among these are the very tight systems LTT 12352 and GJ 866 which have separations much smaller than LTT 1445. The remaining three systems—GJ 2005, GJ 1230, and GJ 1245—all have archival *HST* NICMOS images available. Remarkably, none appears to exhibit the possible co-planarity we observe in LTT 1445ABC.

---

[36] We do not include GJ 799/803 or GJ 569ABC. We consider the primary of the GJ 799/803 system to be a late K-type star, based on the M-dwarf color cuts described by Winters et al. (2019), and we consider one of the companions to GJ 569A to be a brown dwarf, again consistent with Winters et al. (2019). Further, we do not include M-dwarf triples that are subsets of higher-order multiples.

The presence of a transiting planet in this system raises the possibility that the entire system is co-planar, which has intriguing implications for planet formation scenarios.

Young stars form in often densely clustered environments with separations between the stars on the order of hundreds of astronomical units. Dynamical evolution of the cluster could result in capture, leading to binaries with wide separations; however, these stellar components would likely not be co-planar. A more likely formation mechanism is the quasi-static fragmentation of the circumbinary disk as the protostellar core is collapsing, where conservation of angular momentum leads to the formation of an accretion disk (Stahler & Palla 2005). Such a system would possess both circumbinary and circumstellar disks. At apastron, a bound stellar pair would disrupt the circumbinary disk, which would tend toward increased eccentricity in the orbit of the stellar pair. Truncation of any circumstellar disks, and the cessation of accretion onto the primary's disk could truncate both the stellar mass and the masses of any planets around the primary. Given the possible co-planarity of the LTT 1445 system, the low masses of the stellar components, the eccentricity of the orbit of the BC stellar pair, and the presence of the terrestrial planet, it is likely that the system formed from the early fragmentation of an individual protostellar core, and not from later dynamical evolution within the young stellar cluster in which the stars formed.

Previous work leads us to expect that LTT 1445Ab is rocky in composition. Planets with radii less than 1.4 $R_\oplus$ are typically terrestrial in nature (Dressing et al. 2015; Rogers 2015). An Earth-like density for LTT 1445Ab in a circular orbit implies a planetary mass of 2.5 $M_\oplus$ and an RV semi-amplitude of 2.3 m s^{-1}. We expect the mass of the planet to be below 8.4 $M_\oplus$, based on our HARPS data. Additional precise RV observations in the near future will provide a robust mass for the planet; this will allow refinement of its surface gravity, which will serve as an input for atmospheric models.

The planet is not in the habitable zone (HZ) of its star. The conservative inner and outer HZ boundaries for a 1 $M_\oplus$ planet around a star with $T_{\rm eff}$ of 3335 K are 0.093 and 0.182 au, respectively, as calculated from the relations in Kopparapu et al. (2013, 2014). The planet receives 5.6 times the Sun's irradiance from its host star, as its orbital distance brings it closer to LTT 1445A than the annulus of its HZ.

LTT 1445Ab is the nearest planet known to transit an M dwarf and is the most spectroscopically accessible, terrestrial planet detected to date. LTT 1445Ab is a prime target for atmospheric studies due to its large transit depth ($\delta = 0.2\%$) and bright host star ($V_{\rm J} = 11.22$, $I_{KC} = 8.66$, $K_s = 6.50$ mag). It is also the second nearest known transiting planetary system to Earth. Currently, the nearest transiting planetary system is HD 219134bc (Motalebi et al. 2015; Gillon et al. 2017), at a distance of 6.5 pc ($\pi = 153.08 \pm 0.09$ mas; Gaia Collaboration et al. 2018); but while the host star is brighter than LTT 1445A ($K_s = 3.25$ mag), the planetary transit depths are nearly an order of magnitude smaller ($\delta = 0.036\%$ for HD 219134b). In contrast, the multi-planet system TRAPPIST-1 at 12.6 pc exhibits planetary transit depths that are, on average, a factor of three larger than that of LTT 1445Ab, but the host star is faint ($V_{\rm J} = 18.75$, $I_{KC} = 14.10$, $K_s = 10.30$ mag).

There are many opportunities for follow-up studies of LTT 1445Ab. For instance, LTT 1445ABC is particularly favorable for ground-based observations to study the planet's

Table 8
Median Values and 68% Confidence Interval for LTT 1445Ab

Parameter	Units	Values
Stellar Parameters:		A
M_*	Mass ($M_\odot$)	0.256 ± 0.014
R_*	Radius ($R_\odot$)	$0.276^{+0.024}_{-0.019}$
ρ_*	Density (g cm^{-3})	17.3 ± 3.9
$\log g$	Surface gravity (cgs)	$4.967^{+0.061}_{-0.075}$
Planetary Parameters:		b
T_0	Optimal conjunction time (BJD$_{TDB}$)	$2458423.42629\pm^{+0.00044}_{-0.00045}$
P	Period (days)	$5.35882^{+0.00030}_{-0.00031}$
T_{14}	Total transit duration (days)	0.0574 ± 0.0011
R_P/R_*	Radius of planet in stellar radii	$0.0458^{+0.0012}_{-0.0011}$
a/R_*	Semimajor axis in stellar radii	$29.6^{+2.6}_{-2.5}$
b	Transit Impact parameter	$0.29^{+0.23}_{-0.20}$
R_P	Radius ($R_\oplus$)	$1.38^{+0.13}_{-0.12}$
a	Semimajor axis (AU)	$0.03807^{+0.00068}_{-0.00071}$
i	Inclination (degrees)	$89.40^{+0.41}_{-0.46}$
e	Eccentricity	$0.19^{+0.35}_{-0.14}$
ω_*	Argument of periastron (degrees)	-139^{+120}_{-76}
T_{eq}	Equilibrium temperature (K)	433^{+28}_{-27}
K	RV semi-amplitude (m s^{-1})	$2.1^{+1.6}_{-2.0}$
K	RV semi-amplitude (m s^{-1})	<9.3 [$3 - \sigma$ upper limit]
M_P	Mass ($M_\oplus$)	$2.2^{+1.7}_{-2.1}$
M_P	Mass ($M_\oplus$)	<8.4 [$3 - \sigma$ upper limit]
ρ_P	Density (g cm^{-3})	$4.4^{+4.0}_{-4.2}$
ρ_P	Density (g cm^{-3})	<22 [$3 - \sigma$ upper limit]
$\log g_P$	Surface gravity (cgs)	$3.11^{+0.22}_{-0.34}$
$\log g_P$	Surface gravity (cgs)	<3.7 [$3 - \sigma$ upper limit]
Wavelength Parameters:		*TESS*
u_1	linear limb-darkening coefficient	0.195 ± 0.030
u_2	quadratic limb-darkening coefficient	0.427 ± 0.027
A_D	Dilution from neighboring stars[a]	0.000 ± 0.013
Telescope Parameters:		HARPS
γ	Systemic RV (m s^{-1})	-5432.3 ± 2.1
$\dot{\gamma}$	RV slope (m s^{-1} day^{-1})	-0.01275 ± -0.00053
$\ddot{\gamma}$	RV quadratic term (m s^{-1} day^{-2})	$0.00000124 \pm 0.00000040$
σ_J	RV jitter (m s^{-1})	$3.25^{+1.2}_{-0.80}$

Note.
[a] Fixed parameter.

atmosphere, as the blended BC pair may provide a valuable calibration source with the same spectral type as that of the primary star, although its utility as a comparison source may be limited if it is the source of the variation and flaring seen in *TESS*. LTT 1445A is small enough and bright enough that we can collect enough photons in space for transmission spectroscopy. From Kempton et al. (2018), we calculate a transmission spectroscopy metric (TSM) of 40 for LTT 1445Ab, where the TSM is the expected signal-to-noise ratio of transmission spectroscopy observations with *JWST*. This TSM is factors of four and three better than those of 9.15 and 13.7 for LHS 1140b and TRAPPIST-1f, respectively.

Based on the known occurrence rates of planets orbiting M dwarfs, it is unlikely that we will detect a small planet more favorable for atmospheric characterization than LTT 1445Ab. There are 55 mid-to-late M dwarf primaries closer than LTT 1445A. The transit probability of LTT 1445A is 1/30. Assuming that all such stars have rocky planets, then we expect to find roughly one as amenable to follow-up study as

LTT 1445Ab. However, Dressing & Charbonneau (2015) estimate the rate of occurrence of planets less than 1.5 $R_\oplus$ to be 0.43 for orbital periods less than 10 days, in which case we expect that this is indeed the best one. A subtlety is that the Dressing & Charbonneau result pertains to early-type M dwarfs; the occurrence rates for mid-to-late M dwarfs may be higher, and thus we may find one or two more planets like LTT 1445Ab, if we are lucky.

This research made use of EXOPLANET (Foreman-Mackey et al. 2019) and its dependencies (Astropy Collaboration et al. 2013, 2018; Kipping 2013; Salvatier et al. 2016; Theano Development Team 2016; Foreman-Mackey et al. 2017, 2019; Foreman-Mackey 2018; Luger et al. 2019).

Facilities: TESS, MEarth, Gemini:North, FLWO:1.5m (TRES), ESO:3.6m, CTIO:0.9m.

Software: CELERITE (Foreman-Mackey et al. 2017), EXO-FASTV2 (Eastman et al. 2013; Eastman 2017), EXOPLANET (Foreman-Mackey et al. 2019), IDL, IRAF, PYMC3 (Salvatier et al. 2016), PYTHON, STARRY (Luger et al. 2019).

ORCID iDs

Jennifer G. Winters https://orcid.org/0000-0001-6031-9513
Amber A. Medina https://orcid.org/0000-0001-8726-3134
David Charbonneau https://orcid.org/0000-0002-9003-484X
Nicola Astudillo-Defru https://orcid.org/0000-0002-8462-515X
Elliott P. Horch https://orcid.org/0000-0003-2159-1463
Jason D. Eastman https://orcid.org/0000-0003-3773-5142
Eliot Halley Vrijmoet https://orcid.org/0000-0002-1864-6120
Hannah Diamond-Lowe https://orcid.org/0000-0001-8274-6639
Elaine Winston https://orcid.org/0000-0001-9065-6633
Thomas Barclay https://orcid.org/0000-0001-7139-2724
Roland Vanderspek https://orcid.org/0000-0001-6763-6562
David W. Latham https://orcid.org/0000-0001-9911-7388
Sara Seager https://orcid.org/0000-0002-6892-6948
Joshua N. Winn https://orcid.org/0000-0002-4265-047X
Jon M. Jenkins https://orcid.org/0000-0002-4715-9460
Joseph D. Twicken https://orcid.org/0000-0002-6778-7552
Felipe Murgas https://orcid.org/0000-0001-9087-1245
Philip S. Muirhead https://orcid.org/0000-0002-0638-8822
Alan M. Levine https://orcid.org/0000-0001-8172-0453
Sébastien Lépine https://orcid.org/0000-0002-2437-2947
Wei-Chun Jao https://orcid.org/0000-0003-0193-2187
Thierry Forveille https://orcid.org/0000-0003-0536-4607
Gilbert A. Esquerdo https://orcid.org/0000-0002-9789-5474
Courtney D. Dressing https://orcid.org/0000-0001-8189-0233
Christopher J. Burke https://orcid.org/0000-0002-7754-9486
Jose-Manuel Almenara https://orcid.org/0000-0003-3208-9815

References

Adams, F. C., & Laughlin, G. 2006, ApJ, 649, 1004
Astropy Collaboration, Price-Whelan, A. M., SipH ocz, B. M., et al. 2018, AJ, 156, 123
Astropy Collaboration, Robitaille, T. P., Tollerud, E. J., et al. 2013, A&A, 558, A33
Astudillo-Defru, N., Bonfils, X., Delfosse, X., et al. 2015, A&A, 575, A119
Ballard, S. 2019, AJ, 157, 113
Bardalez Gagliuffi, D. C., Burgasser, A. J., Schmidt, S. J., et al. 2019, arXiv:1906.04166
Benedict, G. F., Henry, T. J., Franz, O. G., et al. 2016, AJ, 152, 141
Berta-Thompson, Z. K., Irwin, J., Charbonneau, D., et al. 2015, Natur, 527, 204
Bonfils, X., Almenara, J. M., Cloutier, R., et al. 2018, A&A, 618, A142
Bouchy, F., Pepe, F., & Queloz, D. 2001, A&A, 374, 733
Boyajian, T. S., von Braun, K., van Belle, G., et al. 2012, ApJ, 757, 112
Ciardi, D. R., Beichman, C. A., Horch, E. P., & Howell, S. B. 2015, ApJ, 805, 16
Claret, A. 2017, A&A, 600, A30
Delfosse, X., Forveille, T., Ségransan, D., et al. 2000, A&A, 364, 217
Dieterich, S. B., Henry, T. J., Golimowski, D. A., Krist, J. E., & Tanner, A. M. 2012, AJ, 144, 64
Dieterich, S. B., Henry, T. J., Jao, W.-C., et al. 2014, AJ, 147, 94
Dittmann, J. A., Irwin, J. M., Charbonneau, D., et al. 2017, Natur, 544, 333
Dressing, C. D., & Charbonneau, D. 2015, ApJ, 807, 45
Dressing, C. D., Charbonneau, D., Dumusque, X., et al. 2015, ApJ, 800, 135
Dressing, C. D., Hardegree-Ullman, K., Schlieder, J. E., et al. 2019, AJ, 158, 87
Duchêne, G., & Kraus, A. 2013, ARA&A, 51, 269
Dvorak, R. 1982, OAWMN, 191, 423
Eastman, J., Rodriguez, J. E., Agol, E., et al. 2019, arXiv:1907.09480
Eastman, J., Gaudi, B. S., & Agol, E. 2013, PASP, 125, 83
Eggenberger, A. 2010, EAS Pub. Ser., 42, 19
Foreman-Mackey, D. 2018, RNAAS, 2, 31
Foreman-Mackey, D., Agol, E., Ambikasaran, S., & Angus, R. 2017, AJ, 154, 220

Foreman-Mackey, D., Barentsen, G., & Barclay, T. 2019, dfm/exoplanet: exoplanet, v0.1.4, Zenodo, doi:10.5281/zenodo.2561395
Furlan, E., & Howell, S. B. 2017, AJ, 154, 66
Gaia Collaboration, Brown, A. G. A., Vallenari, A., et al. 2018, A&A, 616, A1
Gillon, M., Demory, B.-O., Van Grootel, V., et al. 2017, NatAs, 1, 0056
Gillon, M., Jehin, E., Lederer, S. M., et al. 2016, Natur, 533, 221
Grimm, S. L., Demory, B.-O., Gillon, M., et al. 2018, A&A, 613, A68
Hambly, N. C., Irwin, M. J., & MacGillivray, H. T. 2001, MNRAS, 326, 1295
Henry, T. J., Jao, W.-C., Subasavage, J. P., et al. 2006, AJ, 132, 2360
Henry, T. J., Jao, W.-C., Winters, J. G., et al. 2018, AJ, 155, 265
Henry, T. J., & McCarthy, D. W., Jr. 1993, AJ, 106, 773
Hirsch, L. A., Ciardi, D. R., Howard, A. W., et al. 2017, AJ, 153, 117
Holman, M. J., & Wiegert, P. A. 1999, AJ, 117, 621
Horch, E. P., Casetti-Dinescu, D. I., Camarata, M. A., et al. 2017, AJ, 153, 212
Horch, E. P., van Belle, G. T., Davidson, J. W., Jr., et al. 2015, AJ, 150, 151
Horch, E. P., Veillette, D. R., Baena Gallé, R., et al. 2009, AJ, 137, 5057
Hosey, A. D., Henry, T. J., Jao, W.-C., et al. 2015, AJ, 150, 6
Howard, W. S., Corbett, H., Law, N. M., et al. 2019, ApJ, 881, 9
Irwin, J., Irwin, M., Aigrain, S., et al. 2007, MNRAS, 375, 1449
Jenkins, J. M., Caldwell, D. A., Chandrasekaran, H., et al. 2010, ApJL, 713, L87
Jenkins, J. M., Twicken, J. D., Batalha, N. M., et al. 2015, AJ, 150, 56
Jenkins, J. M., Twicken, J. D., McCauliff, S., et al. 2016, Proc. SPIE, 9913, 99133E
Kempton, E. M. R., Bean, J. L., Louie, D. R., et al. 2018, PASP, 130, 114401
Kipping, D. M. 2013, MNRAS, 435, 2152
Kopparapu, R. K., Ramirez, R., Kasting, J. F., et al. 2013, ApJ, 765, 131
Kopparapu, R. K., Ramirez, R. M., SchottelKotte, J., et al. 2014, ApJL, 787, L29
Kraus, A. L., Ireland, M. J., Huber, D., Mann, A. W., & Dupuy, T. J. 2016, AJ, 152, 8
López-Morales, M., Ben-Ami, S., Gonzalez-Abad, G., et al. 2019, AJ, 158, 24
Lovis, C., & Pepe, F. 2007, A&A, 468, 1115
Luger, R., Agol, E., Foreman-Mackey, D., et al. 2018, STARRY: Analytic computation of occultation light curves, Astrophysics Source Code Library, ascl:1810.005
Luger, R., Agol, E., Foreman-Mackey, D., et al. 2019, AJ, 157, 64
Luyten, W. J. 1957, A Catalogue of 9867 Stars in the Southern Hemisphere with Proper Motions Exceeding 0″.2 Annually. (Minneapolis, MN: Lund Press)
Luyten, W. J. 1980, NLTT Catalogue, Vol. 3 (Mineapolis, MN: Univ. Minnesota)
MacKnight, M., & Horch, E. P. 2004, AAS Meeting, 204, 07.19
Mann, A. W., Feiden, G. A., Gaidos, E., Boyajian, T., & von Braun, K. 2015, ApJ, 804, 64

Mason, B. D., Wycoff, G. L., Hartkopf, W. I., Douglass, G. G., & Worley, C. E. 2001, AJ, 122, 3466
Matson, R. A., Howell, S. B., Horch, E. P., & Everett, M. E. 2018, AJ, 156, 31
Mayor, M., Pepe, F., Queloz, D., et al. 2003, Msngr, 114, 20
Ment, K., Dittmann, J. A., Astudillo-Defru, N., et al. 2019, AJ, 157, 32
Morley, C. V., Kreidberg, L., Rustamkulov, Z., Robinson, T., & Fortney, J. J. 2017, ApJ, 850, 121
Motalebi, F., Udry, S., Gillon, M., et al. 2015, A&A, 584, A72
Muirhead, P. S., Dressing, C. D., Mann, A. W., et al. 2018, AJ, 155, 180
Muirhead, P. S., Mann, A. W., Vanderburg, A., et al. 2015, ApJ, 801, 18
National Academies of Sciences, E. , & Medicine 2018, Exoplanet Science Strategy (Washington, DC: The National Academies Press)
Neves, V., Bonfils, X., Santos, N. C., et al. 2014, A&A, 568, A121
Pecaut, M. J., & Mamajek, E. E. 2013, ApJS, 208, 9
Ricker, G. R., Winn, J. N., Vanderspek, R., et al. 2015, JATIS, 1, 014003
Rodler, F., & López-Morales, M. 2014, ApJ, 781, 54
Rodriguez, D. R., Duchêne, G., Tom, H., et al. 2015, MNRAS, 449, 3160
Rogers, L. A. 2015, ApJ, 801, 41
Rossiter, R. A. 1955, POMic, 11, 1
Salvatier, J., Wiecki, T. V., & Fonnesbeck, C. 2016, PeerJ Computer Science, 2, e55
Skrutskie, M. F., Cutri, R. M., Stiening, R., et al. 2006, AJ, 131, 1163
Smith, J. C., Stumpe, M. C., Van Cleve, J. E., et al. 2012, PASP, 124, 1000
Snellen, I. A. G., de Kok, R. J., le Poole, R., Brogi, M., & Birkby, J. 2013, ApJ, 764, 182
Stahler, S. W., & Palla, F. 2005, The Formation of Stars (Weinheim: Wiley-VCH)
Stassun, K. G., Oelkers, R. J., Pepper, J., et al. 2018, AJ, 156, 102
Stumpe, M. C., Smith, J. C., Catanzarite, J. H., et al. 2014, PASP, 126, 100
Theano Development Team 2016, arXiv:1605.02688
Thompson, S. E., Fraquelli, D., Van Cleve, J. E., & Caldwell, D. A. 2016, Kepler Archive Manual, Tech. Rep. KDMC-10008-006
Tokovinin, A., Mason, B. D., & Hartkopf, W. I. 2010, AJ, 139, 743
Twicken, J. D., Catanzarite, J. H., Clarke, B. D., et al. 2018, PASP, 130, 064502
Twicken, J. D., Chandrasekaran, H., Jenkins, J. M., et al. 2010, Proc. SPIE, 7740, 77401U
Vanderspek, R., Huang, C. X., Vanderburg, A., et al. 2019, ApJL, 871, L24
Wang, J., Fischer, D. A., Xie, J.-W., & Ciardi, D. R. 2014a, ApJ, 791, 111
Wang, J., Xie, J.-W., Barclay, T., & Fischer, D. A. 2014b, ApJ, 783, 4
Ward-Duong, K., Patience, J., De Rosa, R. J., et al. 2015, MNRAS, 449, 2618
Winn, J. N., & Fabrycky, D. C. 2015, ARA&A, 53, 409
Winters, J., Irwin, J., Newton, E., et al. 2018a, AAS Meeting, 231, 334.06
Winters, J. G., Henry, T. J., Jao, W.-C., et al. 2019, AJ, 157, 216
Winters, J. G., Irwin, J., Newton, E. R., et al. 2018b, AJ, 155, 125